Francke, H., Kraume, M., Saadat, A. (2013): Thermal-hydraulic measurements and modelling of the brine circuit in a geothermal well. - *Environmental Earth Sciences*, *70*, 8, 3481-3495,

DOI: 10.1007/s12665-013-2612-8

Thermal-hydraulic measurements and modelling of the brine circuit in a geothermal well

Henning Francke[1], Matthias Kraume[2], Ali Saadat[3]

Abstract

Wellhead temperature and pressure are critical parameters of a geothermal well. Their prediction requires knowledge of the geofluid properties and detailed thermal modelling of the well and formation. High salinity and gas content complicate the task. This article presents a comprehensive thermal-hydraulic wellbore model, which is parameterized and validated with data from the Gross Schoenebeck site, and used for a long-term prognosis. Geofluid properties are calculated based on the specific gas and salt contents by determining the vapour-liquid equilibrium.

Nomenclature

Abbreviations

GrSk	Gross Schoenebeck (test site)
MSL	Modelica Standard Library 3.2
MD	measured depth
PI	productivity index
TVD	true vertical depth
VLE	vapour-liquid equilibrium

Indices

α,γ	component index
$'/''$	liquid / gaseous
s/g	salt / gas
fw	fluid - wall
wh	wellhead
pi	pump inlet
bot	bottom-hole

[1] GFZ Potsdam
[2] Technische Universität Berlin

res	reservoir
$1/2$	inflow / outflow
is	isentropic
if	interface cement-formation
∞	far-field, at radial outer formation boundary

Symbols

b	molality (amount of solute per mass of solvent) [mol/kg]
C_p	heat capacity [J/K]
c_p	specific heat capacity [J/(kg·K)]
$C_{p,\Phi}$	apparent molar heat capacity [J/(K·mol)]
d	pipe diameter [m]
f	friction factor [-]
g	gravitational acceleration [9.80665 m/s2]
Gr	Grashof number [-]
h	specific enthalpy [J/(kg·K)]
H_Φ^α	apparent molar enthalpy [J/mol]
M	molar mass [kg/mol]
$\dot{m}$	mass flow rate [kg/s]
n	amount of substance [mol]
$N_{s/g}$	number of salts/gases in the geofluid
p	pressure [Pa]
p_{pi}	pump inlet pressure
p_{top}^{ann}	top annulus pressure
PI	well productivity index (in equations basic units [m³/(s·Pa)] are used, values are given the common unit [m³/(h·MPa)])
Pr	Prandtl number [-]
$\dot{q}$	heat flux density [W/m²]
r	radius, measured horizontally from well centre
R	universal gas constant
r_∞	boundary radius of formation model
s	measured length of well-bore starting at inflow [m] (>0)
T	temperature [K]

T_∞	temperature at boundary radius of formation model
T_{pi}	pump inlet temperature
T_{wh}	well head temperature
w	mean flow velocity [m/s]
$\dot{V}$	volume flow rate [m³/s]
V_Φ^α	apparent molar volume [m³/mol]
x	mass fraction of gas phase (steam quality)) [W/(m·K)]
X_α	geofluid mass fraction of component α [kg/kg]
y	mole fraction
z	true vertical depth [m] (<0)
β	thermal expansion coefficient [1/K]
η	efficiency [-]
λ	thermal conductivity [W/(m·K)]
ν	kinematic viscosity [m²/s]
ρ	density [kg/m³]
φ	wellbore inclination, angle to horizontal [-] (φ =90° means normal flow upwards)
ψ	heat transfer coefficient [W/(m²K)]

1 Introduction

Predicting flow parameters for a production well is of central interest for the use of geothermal energy: The wellhead temperature T_{wh} is a critical parameter for the design of the downstream facilities as well as for economic considerations. So is the pressure profile, as it determines power consumption of the pump and the achievable mass flow. Another interesting flow parameter is the volume fraction of the gas phase. A high gas fraction can decrease the pump performance and may require additional or adapted installation, such as a degassing unit, a multiphase pump or pressure maintenance to avoid degassing and thus reduce the injection pumping work load.

Flow in a well is basically a vertical pipe flow, but the applicability of the common hydraulic equations with the assumption of constant density is limited. With the hydrostatic head being the dominant phenomenon, precise density calculation is crucial because estimation errors cumulate over the whole length of the well (Francke and Thorade, 2010). That in turn requires knowledge of the fluid temperature, which is of interest by itself, as stated above. Fluid temperature depends on the heat flow to the formation, which therefore cannot be neglected when modelling geothermal wells (Hasan and Kabir, 2010).

Pioneering work has been done by Ramey (1962) with the development of an analytical solution for wellbore heat transmission. Willhite (1967) contributed with his work about heat transfer

coefficients. Analytical solutions obviously have their limitations, as they require vertically uniform well layouts with constant parameters such as mass flow or thermal properties of formation and geofluid. Furthermore, they are only valid after an initial phase when flow and heat transfer are quasi-static.

The increase of available computing power gave rise to the application of more detailed numerical models (Hasan and Kabir, 2010). They usually focus on one application domain like gas/oil production (Pourafshary et al., 2009), (Livescu et al., 2010), geothermal wells (Guðmundsdóttir, Jonsson and Palsson, 2012) or CO_2 injection (Wiese et al., 2010) and their particular phenomena (heat transfer, two-phase flow regimes, phase transition etc.). A common and obvious approximation for geothermal wells is the use of pure water property functions which is inappropriate for high-salinity brines. Other property models are limited to single chlorides or seawater (i.e. fixed salt composition, mainly sodium chloride), such as Silvester and Pitzer (1977), Millero (2009), Pierrot and Millero (2000), Driesner (2007). Two-phase models are limited to constant gas fractions or single substance flash calculations.

This paper presents a two-phase thermo-hydraulic wellbore model, which is being developed as a PhD project. It includes a multi-salt multi-gas geofluid property model and a detailed heat loss calculation. The wellbore model is applied to the geothermal research site in Gross Schoenebeck (GrSk) (Huenges et al., 2006), validated with field test data and used for long-term prognosis.

Production of geothermal fluid

Geothermal energy can be exploited by pumping hot geofluid from a deep reservoir to the surface by an pump installed in the wellbore (Frick et al., 2011). The well completion consists of steel pipes cemented to the formation in telescope-like layout (Fig. 1). The pump is connected to the production string, a pipe with a smaller diameter centred within the casing and hanging from the top. The surrounding open annulus is connected to the well part below the pump and therefore acts as a fluid buffer during production start-up.

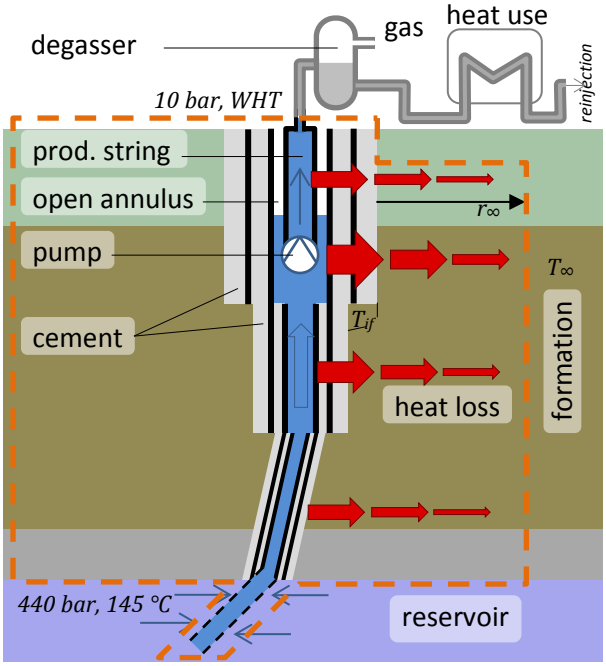

Fig. 1: Schematic view of the geothermal production site in Gross Schoenebeck with well, degasser and heat exchanger, arrows indicating fluid flow and heat flow, dashed box shows model boundary

The natural formation temperature decreases from reservoir to surface, creating a temperature difference to the hot fluid. This temperature gradient causes significant heat loss of the fluid on its way from the reservoir to the wellhead. The heat flow warms up the formation surrounding the well gradually over the years of production. This will reduce the temperature gradient, therefore decrease the heat loss and eventually increase T_{wh}.

The geofluid extracted from the deep aquifer in GrSk contains a high amount of dissolved salts (mostly NaCl, $CaCl_2$, KCl) and gases (mostly N_2, CH_4, CO_2). Due to pressure difference between aquifer and the above ground facility (hydrostatic + friction), degassing occurs during production. The gas fraction influences density and viscosity of the resulting two-phase fluid, which has to be accounted for during pump design. Degassing of CO_2 increases the pH, which can lead to corrosion and precipitation of solids. CO_2 degassing can be limited by maintaining the pressure in the brine circuit above a certain level. In GrSk the gas fraction is removed from the produced fluid before heat extraction in a degasser, which avoids problems in the downstream components like gas accumulation and increased injection pumping work load (Quong et al., 1980).

2 Model description

The purpose of the wellbore model is to simulate the mid-term and long-term hydraulic and thermal behaviour of the geothermal well. It contains sub-models of geofluid, reservoir, formation, pump and of the wellbore itself (Fig. 1). Model boundaries are the well bottom with inflow from the reservoir, the wellhead and the cylindrical outer boundary of the formation around the wellbore. The model allows for quasi-static simulation of well behaviour under varying thermal conditions.

The model has been implemented in Modelica/DYMOLA using MSL 3.2 (Elmqvist, Tummescheit and Otter, 2003) and DYMOLA 2013 (Dassault Systèmes AB, 2013).

2.1 Geofluid model

Density, enthalpy and viscosity of the fluid properties are calculated using a two-phase multi-gas multi-salt model, which reproduces phase transition based on functions of solubility, density and specific heat capacity for aqueous chloride solutions.

For a given p-T-state the fluid model first determines the gas mass fraction x and then the other variables by calculating them separately for both phases and combining them according to x.

The following modelling assumptions have been made about the geofluid:

The fluid consists of water, N_s salts and N_g non-condensable gases; its composition is given by the vector of mass fractions X. There are one or two phases: liquid and, if absolute pressure is low enough, gas. The gas phase is composed of N_g gases and water vapour. The gas mass fraction is defined as the quotient of mass in gas phase and total mass in a given volume:

$$x = \frac{mass\ of\ (gases + water\ vapour)}{total\ mass}. \qquad (1)$$

Salts are completely dissolved in and limited to the liquid phase. Water and gases are exchanged between the liquid and the gas phase by degassing/dissolution or evaporation/condensation. Both

phases are in thermodynamic equilibrium, which is simplified to equality of pressure and temperature in both phases, as well as equality of saturation (degassing) pressures in the liquid phase and the respective partial pressures in the gas phase:

$$p_\alpha^{sat}(p,T,X') = p_\alpha \ , \ \alpha = 1 \dots N_g + 1 \, . \tag{2}$$

Gases dissolve in liquid depending on their respective solubility, which depends on temperature and salt content, but not on the content of other gases. The saturation pressure of water is reduced by the salt content according to Raoult's law (Smith, Ness and Abbott, 2001) proportionally to its mole fraction:

$$y'_{H2O} p_{H2O}(T) = y''_{H2O} p \, . \tag{3}$$

y is the mole fraction in the liquid (') or ('') gas phase.

Gas mass conservation is fulfilled by linking the molar numbers in both phases via the constant total number of moles per fluid mass:

$$n'_\alpha + \ n''_\alpha = n_\alpha \tag{4}$$

Dalton's Law states that the partial pressures p_α are proportional to mole fractions and that they sum up to the absolute pressure:

$$p_\alpha = p \, n''_\alpha \Big/ \sum_{N_g+1} n''_\gamma \tag{5}$$

$$p = \sum_{N_g+1} p_\alpha \ . \tag{6}$$

2.1.1 Vapour-liquid equilibrium (VLE)

According to Duhem's theorem the system is determined by two independent variables, here p and T. Gibbs' phase rule states that it has N_g+1 degrees of freedom. The employed Modelica compiler/solver DYMOLA is capable of solving this equation system as long as it is isolated, but multiple use in the wellbore model required coding the VLE algorithm as a function to enforce the isolation of the problem. The equations are written in matrix form and then solved using the multidimensional Newton's method:

The task is to find the set of normalized gas mole numbers $\tilde{n}''_\alpha = n''_\alpha / n_\alpha$ that fulfils eq. 2 for all α={1…N_{gas}+1}:

$$f_\alpha(\tilde{\boldsymbol{n}}'') = p_\alpha(\tilde{\boldsymbol{n}}'') - p_\alpha^{sat}(\tilde{\boldsymbol{n}}'') \stackrel{!}{=} 0 \, . \tag{7}$$

Using Newton's method $\tilde{\mathbf{n}}''$ can be found by choosing a start vector, iteratively solving the linear system of equations

$$\nabla \boldsymbol{f} \, \Delta\tilde{\boldsymbol{n}}''[k] + \boldsymbol{f}(\tilde{\boldsymbol{n}}''[k]) = 0 \tag{8}$$

for $\Delta\tilde{\mathbf{n}}''[k]$ as the correction vector and determining a new concentration:

$$\tilde{\boldsymbol{n}}''[k+1] = \tilde{\boldsymbol{n}}''[k] + \Delta\tilde{\boldsymbol{n}}''[k] \tag{9}$$

The start vector is set to $\tilde{\mathbf{n}}[0]$={0.5, …, 0.5}, i.e. gases and water are equally distributed between both phases.

Mass compositions of the phases are eventually calculated from the gas mass fraction x with the molar weights M_α as:

$$X'_\alpha = \frac{n'_\alpha M_\alpha}{1-x} \quad X''_\alpha = \frac{n''_\alpha M_\alpha}{x}. \tag{10}$$

2.1.2 Density

The specific volume of the two phase fluid is calculated from the specific volumes of both phases weighted with their mass fraction:

$$\frac{1}{\rho} = v = (1-x)v' + xv'' = \frac{1-x}{\rho'} + \frac{x}{\rho''} \tag{11}$$

Density of the liquid phase is calculated by combining the densities of solutions of single salts, while gas phase density is calculated using the ideal gas law.

Density of the gas phase

For the density calculation the gas phase is assumed to be an ideal mixture of ideal gases. The ideal gas law is used with the specific gas constant of the gas phase R''_s, which is the average of the specific gas constants of gas and water, mass weighted according to the actual composition:

$$R''_s = \sum X''_\alpha \frac{R}{M_\alpha}\ , \tag{12}$$

$$\rho'' = \frac{p}{T \cdot R''_s}\ . \tag{13}$$

The ideal gas law is valid for low densities, where molecule interactions are negligible, whereas pressure and therefore density is rather high at greater depth of the well. The influence of the gas phase there, if present, on the fluid density is, however, negligible there, because due to said pressure the gas phase occupies little or no volume there.

Density of the liquid phase

A density function for different binary aqueous chloride solutions is provided by (Mao and Duan, 2008). Their final equation that converts the apparent molar volume V_Φ^α to solution density ρ is extended to a mixing rule (Laliberté and Cooper, 2004). The respective apparent molar volumes V_Φ^α are combined to yield the density of the multi-salt solution:

$$\rho' = \left(\frac{X'_{H2O}}{\rho'_{H2O}} + \sum_{N_s} X'_\alpha \frac{V_\Phi^\alpha}{M_\alpha} \right)^{-1}\ . \tag{14}$$

Only NaCl[1], KCl[2] and $CaCl_2$[3] are considered here, being the main constituents in the GrSk fluid. The density of pure water used in this approach is provided by the IAPWS/IF97 standard (Wagner et al., 2000) included in the Modelica Standard Library 3.2 (MSL - www.modelica.org).

[1] validity density NaCl: T=273…573 K, p=1…1000 bar and b=0…6 mol/kg)
[2] validity density KCl: T=273…543 K, p=1…500 bar and b=0…4.5 mol/kg)
[3] validity density $CaCl_2$: T=273…523 K, p=1…600 bar and b=0…6 mol/kg)

The liquid density model has been validated (difference < 1 %) against measurements of the ternary solutions NaCl+$CaCl_2$ and KCl+$CaCl_2$ (Zhang, Chen and Han, 1997), as well as against online measurements of the GrSk fluid from the field test referred to in section 5 (Feldbusch et al., 2013).

2.1.3 Viscosity

The viscosity of the liquid phase is assembled from the viscosities of the binary solutions of NaCl, KCl (Mao and Duan, 2009) and $CaCl_2$ (Zhang, Chen and Han, 1997) evaluated for the total molality using a geometric mixing rule weighted by mole fraction among the salts:

$$\eta' = \eta_{H2O} \prod_{N_s} \left(\eta_\alpha \left(p, T, \sum_{N_s} b'_\beta \right) \right)^{\frac{b'_\alpha}{\Sigma_{N_s} b'_\beta}} . \qquad (15)$$

The viscosity of pure water required for this approach is provided by the MSL.

Viscosity of the gas phase is provided by the moist air media model of the MSL (Casas, Prölß and Schmitz, 2005).

2.1.4 Solubility functions

They VLE algorithm makes use of the functions for solubility of N_2 (Mao and Duan, 2006)[1], CO_2 (Duan et al., 2006)[2] and CH_4 (Duan and Mao, 2006)[3] in water. They were developed for NaCl solutions and then extended to solutions of Na^+, K^+, Mg^{2+}, Ca^{2+},Cl^- and SO_4^{2-} with a simple approach based on the ion valence.

2.1.5 Enthalpy

The total specific enthalpy of the fluid is calculated by combining the specific enthalpies of both phases according to their mass fractions:

$$h = x \cdot h'' + (1 - x) \cdot h' \qquad (16)$$

Enthalpies of boundary surface, gas solution and dilution are not considered.

Enthalpy of the gas phase

Enthalpy of the gas phase is modelled as the enthalpy of an ideal mixture of ideal gases, i.e. it is calculated as the mass weighted average of the individual gas enthalpies including water.

$$h'' = \sum_{\alpha=1}^{N_g} h''_\alpha X''_\alpha \quad . \qquad (17)$$

The individual gas enthalpies are calculated using ideal gas functions in the MSL.

[1] validity solubility N_2: T=273…400 K, p=1…600 bar and b=0…6 mol/kg)
[2] validity solubility CO_2: T=273…533 K, p=0…2000 bar and b=0…4.5 mol/kg)
[3] validity solubility CH_4: T=273…523 K, p=1…2000 bar and b=0…6 mol/kg)

Heat capacity and enthalpy of the liquid phase

The influence of adding salt on a fluid can be indicated with the apparent molar property (volume, heat capacity, enthalpy), which denotes the change of that property per added mole of salt. The apparent molar heat capacity $C_{p,\Phi}$ is hence defined as (Spitzer et al., 1978):

$$C_{p,\Phi}^{salt} := \frac{C_{p,brine}(n_{salt}) - C_{p,H2O}}{n_{salt}} \quad \textit{(Unit: J/mol).} \qquad \textit{(18)}$$

Inverting that relation the specific enthalpy of a b-molar solution consequently is:

$$c_p(p,T,\boldsymbol{b}) = \frac{C_{p,H2O}(p,T) + bm_{H2O}\, C_{p,\Phi}^{salt}(p,T,n)}{m_{H2O}(1+bM_{salt})} = \frac{c_{p,H2O}(p,T) + bC_{p,\Phi}^{salt}(p,T,n)}{1+bM_{salt}} \quad . \qquad \textit{(19)}$$

That equation can be easily adapted to handle several salts. Neglecting solvent interactions the specific heat capacity of a multi-salt solution can be estimated with:

$$c_p(p,T,\boldsymbol{b}) = \frac{c_{p,H2O}(p,T) + \sum_{N_s} b_\alpha C_{p,\Phi}^{\alpha}(p,T,n)}{1+\sum_{N_s} b_\alpha M_\alpha} \quad . \qquad \textit{(20)}$$

In analogy to eq. 20 the specific enthalpy of a multi-salt solution is written as

$$h(p,T,\boldsymbol{b}) = \frac{h_{H2O}(p,T) + \sum_{N_s} b_\alpha H_{\Phi}^{\alpha}(p,T,n)}{1+\sum_{N_s} b_\alpha M_\alpha} \quad . \qquad \textit{(21)}$$

The apparent molar enthalpies H_Φ^α are calculated from apparent molar heat capacities by integration:

$$H_{\Phi}^{\alpha}(T) = H_{\Phi}^{\alpha}(T_0) + \int_{T_0}^{T} C_{p,\Phi}^{\alpha}\, dT \quad . \qquad \textit{(22)}$$

The integration constants $H_\phi^\alpha(T_0)$ contain the heats of solution and dilution. They are taken from the literature (Sanahuja and Gómez-Estévez (1986), Sinke, Mossner and Curnutt (1985)). They create a constant offset, which is irrelevant in this application, because only enthalpy differences are used.

This approach also allows the use of the specific enthalpy of an aqueous NaCl solution (Driesner, 2007) instead of water as the basic enthalpy:

$$h(p,T,\boldsymbol{b}) = \frac{(1+b_{NaCl}M_{NaCl})h_{Dr}(p,T,b_{NaCl}) + \sum_{N_s-1} b_\alpha H_{\Phi}^{\alpha}(p,T,n_\alpha)}{1+\sum_{N_s} b_\alpha M_\alpha} \quad . \qquad \textit{(23)}$$

Alternatively expressed with mass fractions:

$$h(p,T,\boldsymbol{b}) = (X'_{H2O} + X'_{NaCl})h_{Dr}\left(p,T,\frac{X_{NaCl}}{X_{H2O}+X_{NaCl}}\right) + X'_{H2O}\sum_{N_s-1} b_\alpha H_{\Phi}^{\alpha} \quad . \qquad \textit{(24)}$$

The apparent molar heat capacities of aqueous $CaCl_2$ and KCl solutions are calculated from a function fitted to the values given in (White et al., 1987) and (White et al., 1987):

$$C_{p,\Phi}^{\alpha}(T,b_\alpha) = \left(b_\alpha^{a_1} + a_2\right)(a_3 - a_4(a_5 - T)^{-1}) \;, \qquad \textit{(25)}$$

The fitting parameters for eq. 25 and 26 are given in Table 1. Integration of the fitting function provides the apparent molar heat capacities required for eq. 23:

$$H_\Phi(T) = H_\Phi^\alpha(T_0) + ((b_\alpha)^{a_1} + a_2)\left(a_3(T - T_0) - a_4\, ln\left(\frac{a_5 - T}{a_5 - T_0}\right)\right) . \quad (26)$$

Table 1: Validity ranges and fitting parameters for apparent molar heat capacity (eq. 25) and apparent molar enthalpy (eq. 26)

	KCl	$CaCl_2$
T_{min} / [K]	*325*	306.8
T_{max}/ [K]	*600*	602.7
p_{min} / [bar]	*164*	21.2
p_{max} / [bar]	*178.8*	178.2
b_{min} / [mol/kg]	*0.1005*	0.1011
b_{max} / [mol/kg]	*3.0073*	3.0284
a_1	*0.09818*	-0.001977
a_2	1.244	-0.9958
a_3	-327.9	1373
a_4	-1.31e+05	6.736e+06
a_5	628.8	628
R^2	0.9759	0.9957

2.2 Reservoir model

The reservoir is represented in the model by a mass flow source and a flow resistor. The source has a predefined mass flow with constant composition, predefined temperature and predefined pressure. The resistor creates a pressure drop proportional to the extracted volumetric flow rate. The proportionality factor is called productivity index. It is defined as the volume flow rate divided by the difference between the static and the steady-state flowing bottom-hole pressure (Haider, 1937). The bottom-hole pressure p_{bot} is hence calculated from the static reservoir pressure p_{res} with eq. 27.

$$p_{bot} = p_{res} - PI \cdot \dot{V} \quad . \quad (27)$$

2.3 Wellbore model

The wellbore model consists of several sections, each one having constant geometrical parameters such as length, diameter, inclination and number of elements. The flow is modelled as being one-dimensional, quasi-stationary and homogeneous, but having two phases. That means, a uniform velocity, pressure and enthalpy is assumed for both phases on a cross-section. As it is discretized using a finite difference forward-space scheme, every section is sub-divided in equidistant elements. On each element balances of mass, energy and momentum are calculated.

The assumption of homogenous flow neglects the hydraulic and thermal effects of slip. Slip increases the static pressure head by reducing the cross section occupied by the gas flow and thus increasing the weight of the fluid column. Besides, heat from the inner friction of the fluid (between the phases) increases the fluid enthalpy. Slip increases with gas volume fraction. So does the error induced by neglecting slip.

Slip calculation is complex as it depends on the flow pattern. However, its influence on the pressure head is included in the two-phase friction model by Friedel (1978). The heat generated by inner friction is negligible.

For the heat flow calculation the well sections are assigned constant thermal parameters, namely diameters and thermal conductivities of several layers of steel, cement and gas or liquid in the

annulus. Heat flow within the well completion is also modelled as quasi-stationary, while heat flow in the formation is modelled as transient.

2.3.1 Mass balance

The mass balance for stationary flow delivers the continuity equation. Mass flow at inlet 1 equals negative mass flow at outlet 2:

$$0 = \dot{m}_1 + \dot{m}_2 \tag{28}$$

2.3.2 Momentum balance

The momentum balance reduces to a pressure balance, showing that the pressure gradient is composed of three parts: hydrostatic, friction and kinetic gradient:

$$\frac{\partial p}{\partial s} = -g \cdot \rho(p,T)\, sin\, \varphi - f\, \frac{w^2 \rho}{2d} - \cancel{\frac{\partial}{\partial s} \rho w^2} \tag{29}$$

s is the measured length, running along the well and increasing in flow direction. The hydrostatic part depends on the well inclination φ and the gravitational acceleration g. Friction depends on flow velocity w, the pipe diameter d and the dimensionless friction factor f.

Setting element density ρ_m=ρ_1 and neglecting the here insignificant kinetic gradient in order to avoid an implicit equation gives:

$$p_2 = p_1 - g\rho_1\, sin\, \varphi\, \Delta s - f\, \frac{w^2 \rho_1}{2d}\, \Delta s \tag{30}$$

f is calculated with the empirical equation for two-phase pipe flow by Friedel (1978). It requires the viscosity of both phases, which are provided by the geofluid model (2.1.3).

2.3.3 Energy balance and heat flow

Assuming that the heat flow causes much faster temperature changes in the well-bore completion than in the formation (Ramey, 1962) and considering the time-scale of interest (> 1h), the heat flow in the well-bore is described by steady-state equations with transient boundary conditions, whereas in the formation transient heat conduction equations are applied.

The energy balance for one well element shows that the change of specific fluid enthalpy is in balance with the radial heat conduction and the change of kinetic energy and of geodetic height:

$$\dot{m}\left(h_2 - h_1 + gsin\varphi \Delta s + \cancel{\frac{w_2^2 - w_1^2}{2}}\right) = \dot{q}\pi d \Delta s \tag{31}$$

Analogous to the momentum balance, the kinetic part is neglected.

Heat flow to/from the formation depends on the heat transfer coefficient of the conducting elements and the respective temperature difference. Here it is calculated between fluid temperature T and interface well-formation T_{if} over several layers of the well completion.

Static cylindrical heat transfer

Steady state heat conduction in a long cylinder with a thin wall and constant thermal conductivity λ can be calculated as (Çengel, 2002) :

$$\dot{Q} = -2\pi \Delta s \frac{\lambda}{ln(R/r)} \big(T(R) - T(r)\big) \tag{32}$$

with Δs being length of cylinder and r/R being the inner/outer radius of cylinder.

Dividing by a lateral surface at a reference radius and introducing a heat transfer coefficient ψ gives an expression for the heat flux on the reference surface:

$$\dot{q}_{ref} = \frac{\dot{Q}}{2\pi\Delta s r_{ref}} = -\frac{\lambda}{ln(R/r)\cdot r_{ref}}\,\Delta T = -\psi^{ref}\cdot\Delta T \quad . \tag{33}$$

ψ^{ref} is the cylindrical heat transfer coefficient with respect to the reference surface A_{ref} at the radius r_{ref}.

Multi-layered cylinders

Multi-layered cylinders can be seen as thermal resistances in series. With the thermal resistance being the inverse of the heat transfer coefficient, their total heat transfer coefficient is calculated like electrical resistors in series by adding the resistances:

$$\dot{q}_{ref} = -\psi_{tot}^{ref}\cdot\Delta T = -\left(\sum\frac{1}{\psi_j^{ref}}\right)^{-1}\cdot\Delta T \quad . \tag{34}$$

Including the coefficient for the heat transfer from the fluid to the pipe wall ψ_{fw} (referring to the hydraulic diameter $2\cdot r_1$) the static heat flux through the interface $\dot{q}_{if}$ is hence calculated as:

$$\dot{q}_{if} = -\left(\frac{r_{if}}{\psi_{fw}^{r_1} r_1} + r_{if}\sum\frac{ln(r_{j+1}/r_j)}{\lambda_j}\right)^{-1}\cdot\left(T_{if} - T_{fluid}\right) \tag{35}$$

λ_j are the thermal conductivities of the layers. r_j are the radii of the layer interfaces. $\dot{q}_{if}$ and T_{if} are exchanged with the formation model. ψ_{fw} is calculated for a turbulent flow (Gnielinski, 1995).

Open annulus

Heat transfer through the open annulus around the production string is strongly influenced by the liquid level, because heat conduction is much higher in liquid brine than in gas. The liquid level is found where annulus fluid pressure p^{ann} equals top annulus pressure p_{top}^{ann}. p^{ann} is calculated from the pump inlet pressure p_{pi} by integrating static pressure head at in-situ temperature upwards from the pump:

$$p_{i+1}^{ann} = max\left(p_{top}^{ann}, p_{pi} - \sum_{i=1}^{j}\rho(p_i^{ann}, T_i^{ann})g(z_{i+1} - z_i)\right) . \tag{36}$$

Furthermore, the heat transfer can be substantially increased by free convection driven by the temperature difference. An equation by Willhite (1967), adapted to temperatures in Kelvin, is used to estimate its influence for both liquid and gas in the annulus:

$$\frac{\lambda_c}{\lambda} = 0.0596(GrPr)^{0.333}Pr^{0.074} \quad . \tag{37}$$

λ is the thermal conductivity of the annular fluid, while λ_c is the effective one, increased by convection.

λ and c_p of the annulus gas are provided by the simple air media model of the MSL 3.2. λ of the annulus liquid (completely degassed brine) is taken from the water model of the MSL 3.2 as salinity dependence is weak for λ compared to c_p (Yusufova et al., 1975).

Gr and Pr are the Grashof and the Prandtl number, defined as:

$$Gr = (R_o - R_i)^3 g\beta |T_i - T_o|/\nu^2 \quad \text{and} \tag{38}$$

$$Pr = \frac{c_p \eta}{\lambda} , \tag{39}$$

where $R_{i/o}$ and $T_{i/o}$ are the inner/outer radius and inner/outer temperature of the annulus and ρ, η, c_p, β are the density, dynamic viscosity, specific heat capacity, thermal expansion coefficient of the fluid.

The isobaric thermal expansion coefficient for ideal gases is $\beta = 1/T$; for liquid it is calculated from density.

2.4 Formation model

The formation is represented by a vertical array of transient 1D-models of conductive radial heat flow with no heat flow and given temperature on the outer boundary. It is coupled to the well-bore model via temperature and heat flow on the interfacing boundary. Vertical heat flow is not considered. Thermal properties are horizontally constant and vertically piecewise constant, considering the detailed lithology. Vertical discretization is the same as in the wellbore model.

The radial extension of the formation model has to be large enough, so that there is no heat flow at the outer boundary within simulation time.

The equation for one-dimensional transient radial heat conduction without heat generation (Çengel, 2002)

$$\rho c_p \frac{\partial T}{\partial t} = \frac{1}{r}\frac{\partial}{\partial r}\left(\lambda(T) r \frac{\partial T}{\partial r}\right) \tag{40}$$

is radially discretized using the Finite Volume Method, which, compared to Finite Differences, creates much smaller discretization error and allows for simpler handling of a non-constant conductivity and a non-equidistant grid:

$$\rho c_p \frac{\partial}{\partial t} T_i = \frac{4}{(2r_i + r_{i+1} + r_{i-1})(r_{i+1} - r_{i-1})} \left(\lambda_+ \frac{r_i + r_{i+1}}{r_{i+1} - r_i} (T_{i+1} - T_i) - \lambda_- \frac{r_{i-1} + r_i}{r_i - r_{i-1}} (T_i - T_{i-1}) \right). \tag{41}$$

with

$$\lambda_i^{\pm} = \lambda\left(\frac{T_i + T_{i\pm1}}{2}\right) . \tag{42}$$

The outer boundary condition is constant temperature, i.e. the far field formation temperature. The inner boundary condition is the heat flow obtained from the wellbore model. It is implemented as

$$\dot{q}_{if} = -\lambda\left(\frac{T_1 + T_2}{2}\right)\frac{T_2 - T_1}{r_2 - r_1}\frac{r_1 + r_2}{2r_1} . \tag{43}$$

Temporal discretization is handled by the Modelica compiler/solver.

2.5 Pump model

The pump is modelled as non-isentropic with a given isentropic efficiency η_{is}:

$$\eta_{is} = \frac{h_1 - h_{2,is}}{h_1 - h_2} \tag{44}$$

The efficiency η_{mot} accounts for the losses of the electric motor. The losses of both pump and motor heat up the fluid. Assuming constant density, the enthalpy difference generated by the pump is therefore:

$$h_2 - h_1 = \frac{p_2 - p_1}{\rho_1 \eta_{is} \eta_{mot}} \quad . \tag{45}$$

The pump model includes a simple controller that adjusts the pump head so that an input pressure value (here wellhead pressure) converges to a pre-set target value.

3 Comparison to analytical solution

An analytical solution for the transient wellbore heat transmission was proposed by (Ramey, 1962). It is based on the assumption of a line source and is therefore not valid close to the well and for short times. It was applied to a simple test case and compared to the results from the wellbore model described before. In the test case 10 kg/s of pure water of 100 °C is produced from a depth of 1000 m through the formation (L07 from Table 4) with a temperature gradient of 3 K/100 m and a surface temperature of 8 °C. Pipe friction and gravitation have been deactivated to eliminate pressure influence on the specific heat capacity, which is constant in the analytical solution.

Fig. 2a and Fig. 2b show very good accordance for time after 1 day, the final difference amounts to 0.2 K.

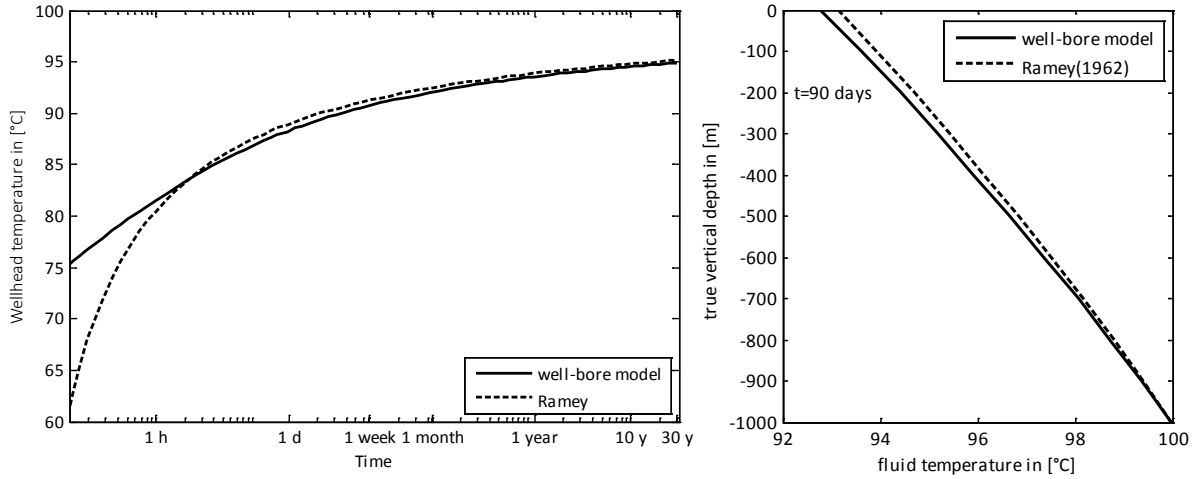

Fig. 2: Comparison of simulated wellhead temperature with analytical solution (Ramey, 1962): a) Wellhead temperature over 30 years. b) Fluid temperature profile after 90 days

4 Model parameters

4.1 Well parameters

The layout of the well GrSk 4/05 is depicted in Fig. 3a. The well consists of 4 sections with different diameters. The indicated diameters are outer diameters of casing, liner, tubing or borehole/cement. The annulus between casing and formation (borehole diameter) is filled with cement. The diameters decrease with depth, because one section has been drilled through the cemented casing of the

previous section. The depths are displayed in true vertical depth and measured depth (along the borehole). The production string connects the pump with the wellhead.

The thermal conductivities of the well casing, liner and tubing are assumed to be 50 W/(m·K), which is an average for carbon steel (Dubbel, 2001). It can vary over a broad range, but as it is much higher than the one of cement and formation, its influence on the heat flow is marginal (see eq. 35). The thermal conductivities of the cement layers have been estimated based on the densities indicated in Fig. 3a via the ρ-λ-relation by (Nelson, 1986). The values are given in Table 2.

Table 2: thermal conductivities of cement determined from densities with (Nelson, 1986)

cement density	thermal conductivity
1450 kg/m³	0.76 W/(m·K)
1650 kg/m³	0.98 W/(m·K)
1925 kg/m³	0.76 W/(m·K)
2000 kg/m³	1.38 W/(m·K)

The borehole diameters d'_{if} are actually larger than the indicated drill diameters d_{if} due to washout[1]. That increases the volume of the annulus between casing and formation by w=8…15 % in the GrSk scenario. This is taken into account in the parameterization by increasing the borehole diameter according to eq. 46 with w=11.5 %.

$$d'_{if}{}^{2} = d_{if}{}^{2}(1+w) \ . \qquad (46)$$

Fig. 3b shows the depths of the geological layers L01 to L11. Their properties are listed in Table 4.

[1] Irregular cavities washed out by the circulating drilling fluid

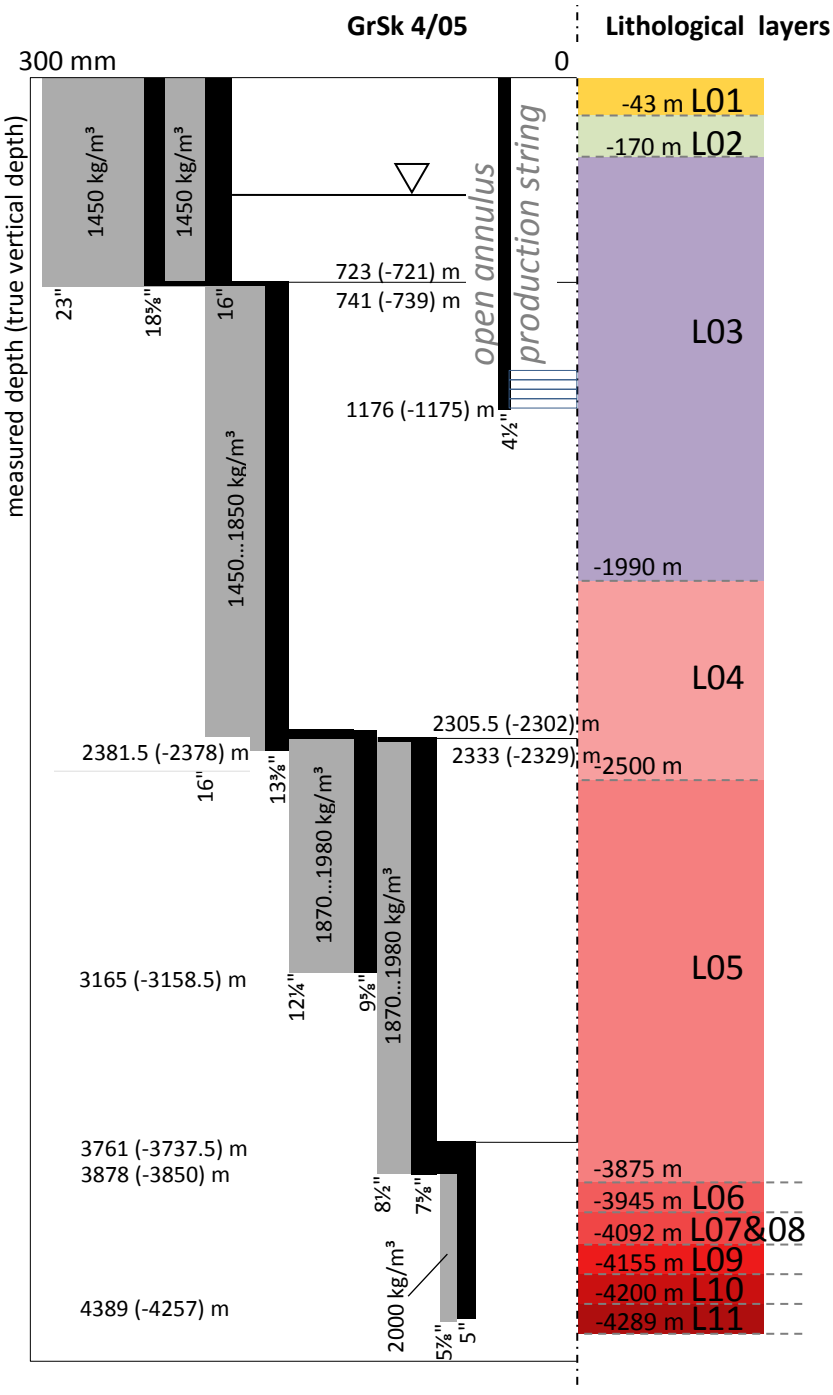

Fig. 3: Wellbore schema (a) and stratigraphy (b) for production well GrSk4 in Gross Schoenebeck (black areas symbolize steel casing/liner/tubing, grey stands for cement)

4.2 Reservoir parameters

The temperature in the reservoir is assumed to be 145 °C (Henninges et al., 2012) and the initial reservoir pressure is assumed to be 44 MPa (Blöcher et al., 2008).

The productivity index PI is estimated to be 1.8 m³/(h·MPa).

4.2.1 Medium properties

The main salts and gases in the GrSk geofluid are considered, representing 99 % wt. of the total dissolved solids and 99 % wt. of the gases. The geofluid salinity is up to 265 g/L, it is nearly saturated with respect to $CaCl_2$ and NaCl, which together make up 98% of salt mass (Regenspurg et al., 2010).

Gas solubility is decreased by salinity to 40 % of that of pure Water (Wiersberg, Seibt and Zimmer, 2004). The volume ratio gas-liquid at 1 atm and 0 °C is approximately 1:1. The gas part is composed mainly of nitrogen (ca. 80 vol. %) and a small part of methane (ca. 15 vol. %) and carbon dioxide (ca. 4.7 vol. %).

The detailed medium composition, derived from measurements (Wiersberg, Seibt and Zimmer, 2004) is given in Table 3.

Table 3: Composition of geofluid produced in Gross Schoenebeck acc. to (Wiersberg, Seibt and Zimmer, 2004)

Component	NaCl	KCl	$CaCl_2$	CO_2	N_2	CH_4	H_2O
Mass fractions	$81.1 \cdot 10^{-3}$	$4.72 \cdot 10^{-3}$	$125 \cdot 10^{-3}$	$169 \cdot 10^{-6}$	$734 \cdot 10^{-6}$	$65.6 \cdot 10^{-6}$	0.788

4.3 Formation parameters

The constant boundary temperature is applied at a radius of r_∞=8 m, which is beyond the range of thermal influence of the well within 1 week, as the simulation shows. The formation temperature (initial and far-field) is based on a measured temperature log (shown as T_∞ in Fig. 6). Seasonal influence is not considered, because it reaches only a few metres into the ground (Scheffer et al., 2009).

4.3.1 Stratigraphy – Thermal parameters of formation

Thermal parameters, depths and thicknesses of the formation layers used in the well-bore model are listed in Table 4.

Table 4: Stratigraphy of GrSk site - thermal parameters. layer definition (Ollinger et al., 2010) and thermal conductivity λ under normal temperature, pressure and saturated conditions (Norden, Förster and Balling, 2008). Thermal capacity c_p by (Norden et al., 2012) and density (Norden, Förster and Balling, 2008)

bottom of [m] (TVD)	**layer**		λ_{20} [W/(m·K)]	c_p [J/(kg·K)]	ρ [kg/m³]
-43	L01	Silts and mudstones	1.8	1029	2100
-170	L02	Sand- and siltstones, with calcareous sandstones in the upper part	2	1000	2300
-1990	L03	Siltstones, marls and sandstones	2.2	902	2540
-2500	L04	Evaporites (mainly halite)	4.5	1060	2160
-3875	L05	Evaporites, mainly anhydrite and carbonates	4.5	746	2600
-3945	L06	Siltstones/mudstones/fine sandstones	2.6	746	2600
-4030	L07	Sandstones	3.5	838	2600
-4092.5	L08	Sandstones	3.5	838	2600
-4155	L09	Sandstones	4	838	2600
-4200	L10	Conglomerates and sandstones	3.8	838	2600
-4300	L11	Andesites	2.3	981	2650

The thermal conductivity changes with pressure and temperature. Pressure influence is neglected, because it is relatively small compared to temperature dependence (Schön, 2004). Temperature influence is taken into account according to (Somerton, 1992):

$$\lambda(T) = \lambda_{20} - 10^{-3}(T - 293)(\lambda_{20} - 1.38)\left(\lambda_{20}(1.8 \cdot 10^{-3}T)^{-0.25\lambda_{20}} + 1.28\right)\lambda_{20}^{-0.64} . \quad (47)$$

4.4 Pump parameters

The efficiency of the electric motor η_{mot} is set to 0.9, a typical value for electric motors. The isentropic efficiency η_{is} is set to 0.7, the minimum value in the operating range according to the data sheet for the installed production pump Centrilift 44-675 HC12500.

5 Model validation with field data

The wellbore model has been validated with a pump test that has been conducted at the GrSk site. In the spring of 2012 production was maintained continuously for 163 h. In the months before there have been only short periods (<12 h) of operation, which is why the formation temperature is assumed to be in the undisturbed stated represented by the temperature profile for T_∞.

5.1 Measured quantities

Among the quantities that were measured and recorded the following ones were selected for model input and comparison with values calculated by the model:

- The volume flow rate $\dot{V}$ has been measured after the degasser (Fig. 4). It was converted to mass flow with the in-situ density and used as source mass flow in the model.
- Wellhead pressure has been measured and was averaged (=9.2 bar) and used as target value for the pump control.
- Temperatures, measured at production pump inlet (T_{pi}) and at the well head (T_{wh}), were compared to calculated data.
- Pressure at production pump inlet has been measured and was used to calculate the PI (see eq. 48).

The PI is not assumed to be constant, but time dependent in order to mirror the transient behavior of the reservoir interacting with the well. It is calculated from the measured values using this equation:

$$PI = \dot{V}/(p_{res} - \bar{\rho} g (z_{ESP} - z_{res}) - p_{in}^{ESP}) \quad , \tag{48}$$

where $\bar{\rho}$ is the average density below the pump and was assumed to be 1136 kg/m³.

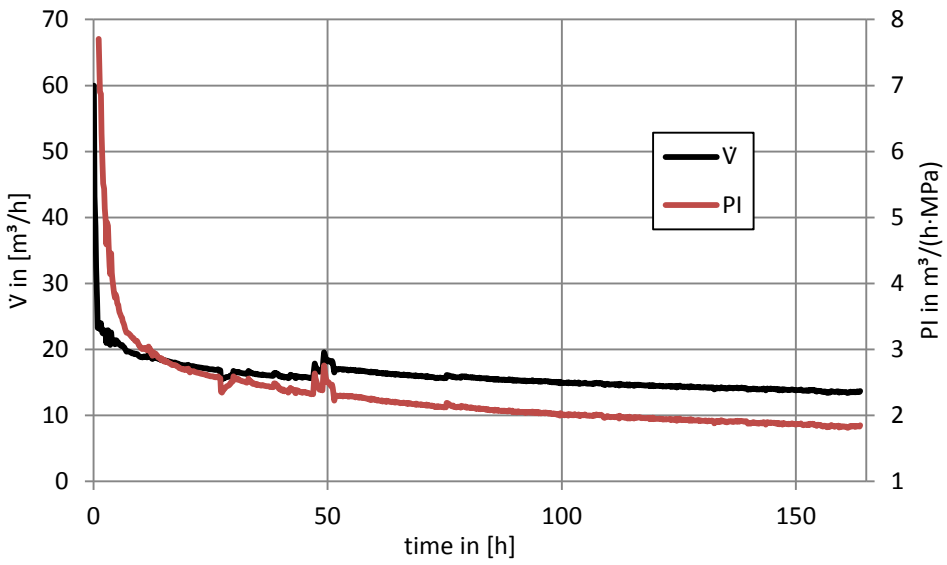

Fig. 4: Measured volume flux $\dot{V}$ after degassing and calculated productivity index *PI*

5.2 Validation with measured temperatures from pump test

The comparison of measured and calculated T_{wh} and T_{pi} is shown in Fig. 5. Only data with t>10 h has been used and plotted in order to exclude dynamic effects such as hydraulic start-up as well as thermal storage in the well completion and in the fluid. The fluid column, initially being approximately in thermal equilibrium with the formation, has to be exchanged once before the assumption of quasi-static flow is justified. According to the recorded data the wellbore volume of about 233 m³ (including the open annulus, see Fig. 3) has been produced after 10.3 h.

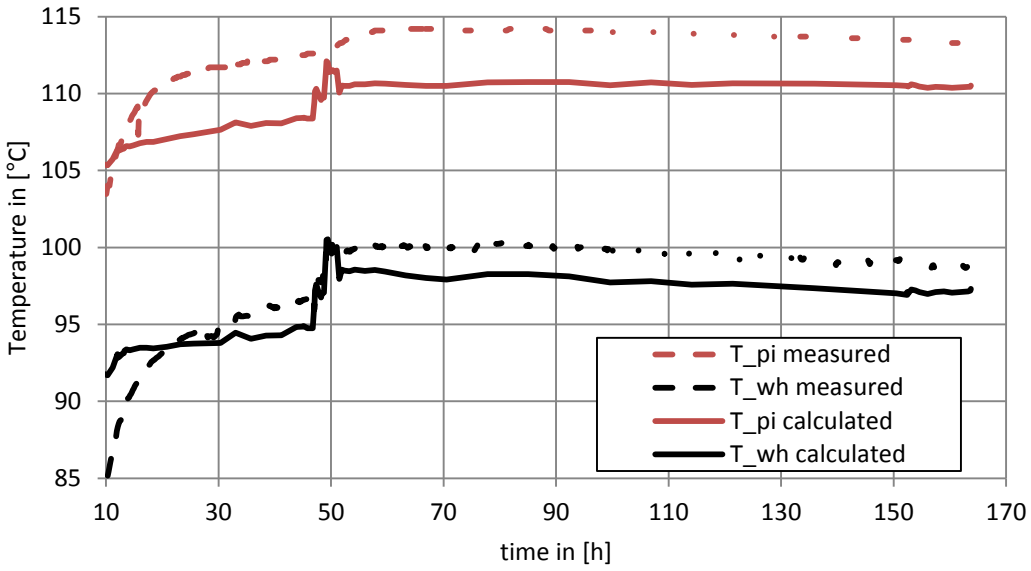

Fig. 5: Pump inlet temperature (T_{pi}) and well head temperature T_{wh}, comparison of measured and calculated values during 7 days pump test, steps in T_{wh} are due to discrete change of annulus water level

After the initial phase of around 24 h the average/final temperature difference amounts to 2.9/2.8 K (T_{pi}) and 1.2/1.6 K (T_{wh}) with calculated temperatures being lower than the measured ones. The temperature drop in the well below the pump is overestimated while above the pump it is underestimated. The overestimation can be qualitatively explained with the fact that the formation has not been undisturbed before the pump test, as assumed for the far-field formation temperature. Furthermore, the real heat flow can be expected to be reduced by potentially imperfect contact of interfaces steel-cement and cement-formation.

The underestimation of the heat loss in the upper well is probably related to uncertainties in the estimation of the free convection in the open annulus and the chemical state of the annulus fluid. They are added to the general uncertainties from the geofluid property calculation, the thermal parameters of cement and formation, and in the measurements themselves. Unconsidered phenomena, such as inhomogeneities in the formation or cement, scaling or corrosion on the pipes, recirculation or slip in the two phase flow may also have their effect on the measured temperatures.

The peak in production rate at t=50 h causes a temperature step, which is much more pronounced in the simulated data than in the measurements. Dampening by heat storage in well completion and the gradual exchange of the fluid column, which are not reproduced by the quasi-static wellbore model, may be responsible for smoothing out the measured temperature curves.

The measured temperatures in Fig. 5 decrease for 50 h<t<165 h due to the decreasing production rate. When mass flow has fallen low enough, less heat flows from fluid to the pipe wall than from there to the formation. The temperature decline is reproduced by the model.

The transient temperature development during the seven days pump test could be reproduced by the model described here with a reasonable error. This was obtained with a rather high level of detail of the wellbore model, because preliminary calculations with simpler models revealed the need for refinement. The influence of free convection both above and below the annulus water level on the heat loss is considerable, as it increased the heat flux by one order of magnitude. Ignoring it leads to an overestimation of the well head temperature of several degrees in the initial phase. The rather simple radially symmetric conductive thermal model of the formation seems to be sufficient.

6 Model application

The wellbore model is used to provide profiles of temperature and gas fraction as well as a long-term prognosis of the wellhead temperature.

6.1 Temperature profile

Fig. 6 displays the calculated temperatures of the fluid, the annulus, the well-formation interface and the formation boundary as well as the heat flux per length unit along the well. It shows the location and the amount of the fluid's heat loss to the formation. It also exhibits the cooling effect of the open annulus where it is filled with liquid and the insulation effect above the liquid level.

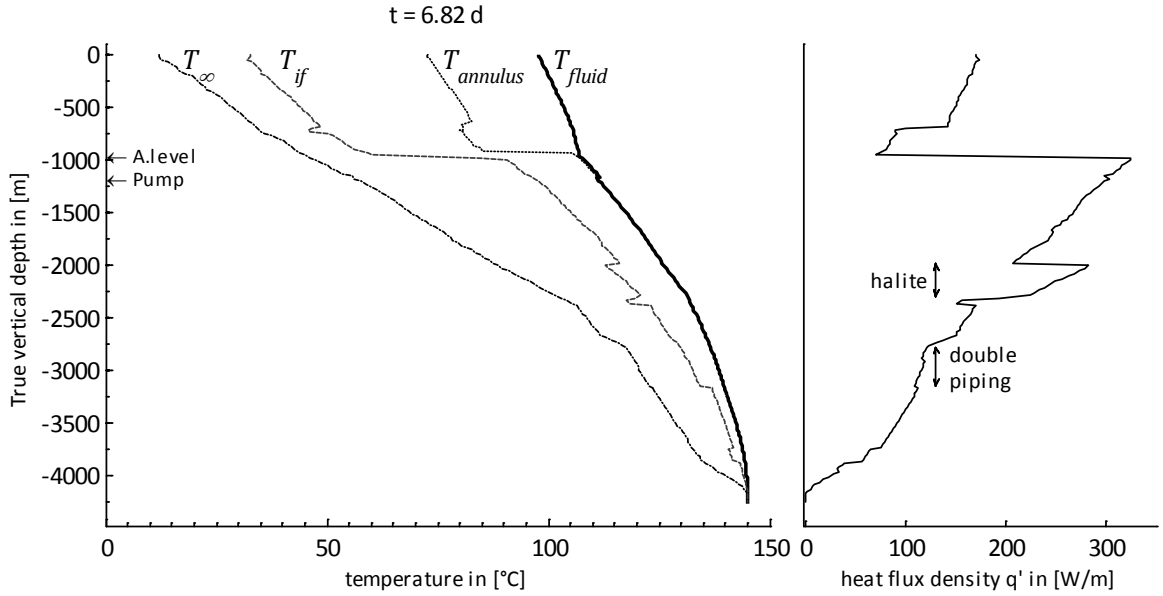

Fig. 6: Simulated temperature profiles of fluid (T_{fluid}), interface well-formation (T_{if}), annulus ($T_{annulus}$) and far field formation (T_∞) as well as profile of heat flux density at the end of the pump test

Heat flow increases generally with the growing temperature difference between fluid (T_{fluid}) and formation (T_∞), but varies with borehole layout and lithology. The liquid level in the annulus is clearly marked by the distinct drop of heat flow at -957 m. Comparison with the well layout (Fig. 3a) reveals that between -3158 and -2738 m heat flow is slightly reduced by the double piping with its double cementation while between -2302 m and -1990 m heat flow is increased by single piping in a halite layer with high thermal conductivity. While the interface temperature T_{if} is roughly in the middle

between (T_{fluid}) and formation (T_∞) below the liquid level in the open annulus, it is close to T_∞ in the part above.

6.2 Degassing

Identifying the location of degassing is interesting with regards to the pump performance, which can be decreased by a high gas fraction. A gas fraction profile, as shown in Fig. 7, may help in choosing the installation depth of a pump.

According to the calculation for the GrSk site, fluid pressure falls below the degassing pressure of 262 bar (at 131°C) initially at 3068 m (TVD). The degassing point, i.e. the first occurrence of a gas bubble, sinks due to the rising temperature, eventually reaching 3322 m.

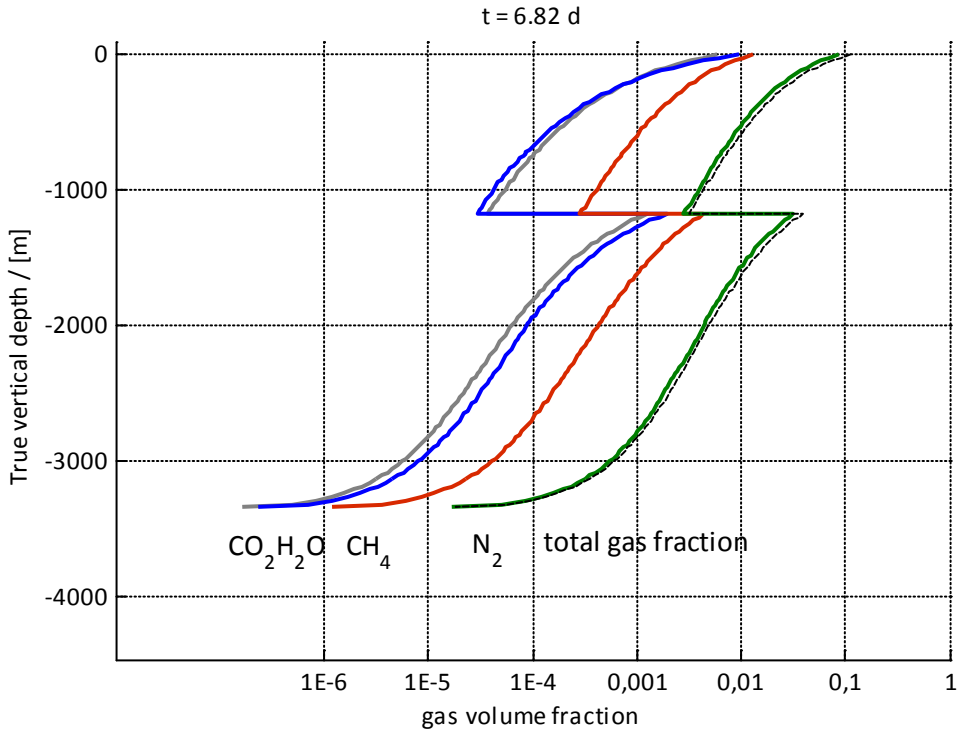

Fig. 7: Simulated profiles of gas volume fractions of total gas phase, N_2, CO_2, CH_4 and water vapour at the end of the pump test

The total gas volume fraction reaches a maximum of 11 % at the wellhead where the minimum pressure is reached. Nitrogen degasses first and dominates the gas phase. The pressure increase at the pump causes re-dissolution of gases and re-condensation of water. Noteworthy is that CO_2 below the pump has a lower partial pressure (or void fraction) than water, but a higher one above. The pressure increase at the pump does not restore the conditions from a depth of approx. 2300 m, where pressure is the same as at the pump outlet, because of the different temperature dependence of the CO_2 degassing pressure and the water vapour pressure.

In the VLE model, as soon as there is a gas phase in partial pressure equilibrium, all gases are partially degassed, even if only very little. Therefore a threshold has to be set in order to determine degassing points for the gases separately. The arbitrary gas fraction threshold of 10^{-4} is exceeded by N_2 at -3270 m, by CH_4 at -2680 m, by H_2O at -1946 m and again at -627 m, and by CO_2 at -1800/ 741 m (Fig. 7).

6.3 Long term temperature prognosis

Setting the simulation time to 30 years, the production rate constant to $\dot{V}$ = 25/50/75/100 m³/h and the productivity index to PI=15 m³h^{-1}/MPa (projected parameters) yields the T_{wh} prognosis given in Fig. 8. The T_{wh} does not reach a stationary level because the formation continues to absorb heat, although at a decreasing rate.

The calculations show, that, with regard to thermal output with respect to a reference temperature $P_{th}=\dot{m}\cdot(h(T_{wh})-h(T_{ref}))$, a higher production rate is desirable not only because of the larger mass flow itself, but also because of the higher achievable T_{wh}. The reason is that a higher mass flow is cooled less by the upper formation, because it will flow faster and remain shorter in the well. But it also brings more heat to the formation, thus warming it up quicker and consequentially shortening the initial warm-up phase. This reduces the temperature range covered by the T_{wh} in the operation time and shortens the heat consumer's operation time at off-design temperature.

T_{wh} prognosis can be used to select the design temperature according to the (limited) production rate and the expected operation time and to estimate the duration of the warm-up phase.

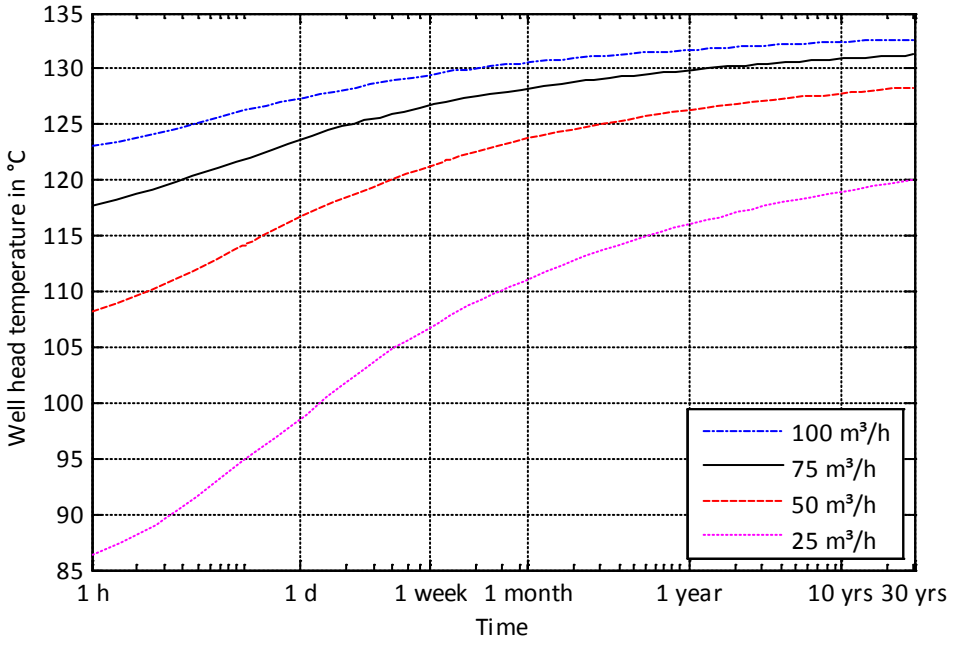

Fig. 8: Prognosis of wellhead temperature for 30 years for a volume flow rate of 25, 50, 75 and 100 m³/h

7 Conclusion and Outlook

7.1 Summary

A comprehensive approach to modelling a geothermal wellbore with potential two-phase flow has been presented and tested. It can be used to predict flow parameters that are essential in the design and dimensioning of the components of the brine circuit, such as the production pump, heat exchanger and the potentially connected power cycle. This model is applicable to geofluids with high gas contents and high salt contents, as it features a detailed two-phase multi-gas multi-salt geofluid property model, capable of reproducing phase transition by degassing/dissolution and

evaporation/condensation. Heat loss to formation is considered with attention to the thermal formation parameters and their dependence on depth and temperature.

The model can predict the temperature development for shorter (i.e. after start-up – few days) and longer periods (i.e. design operation time – e.g. 30 years) with different parameters and make statements about the heat available to the attached heat consumer. It can provide profiles of fluid properties such as temperature, pressure, density, gas fraction (degassing point) as well as heat flow to formation and formation temperature in various distances from the well.

7.2 Future work

Future work will involve further validation, evaluation, refinement and extension of the model.

After the thermal validation presented here, the next steps are the comparison of the hydraulic values and gas fraction with measured data. Chemical modelling software (e.g. PHREEQC, ProSim Simulis) is available that may be capable of reproducing the geofluid properties. It could be used to validate or even replace the geofluid model described here.

Distributed Temperature Sensing measurements, similar to ones described by Reinsch et al. (2013), were performed during the pump test described here. These temperature profiles will be compared to simulation results.

Accordance with measured values during sudden changes of production rate can be improved by including the thermal heat storage in the well completion and a non-steady-state thermal flow model. Use of a refined pump model considering the pump characteristics and load dependent efficiency is envisaged. More detailed two-phase flow modelling (slip, flow regimes) may be necessary when simulating higher void fractions.

Sensitivity analyses will be conducted to identify possibilities of model simplification and optimization of operation.

Geofluid inflow to the well from the reservoir has been simplified to happen at one depth in the model of the GrSk site. Modelling more in detail the real confluence from several horizons with different temperatures and different productivities as well as their hydraulic interaction could help in understanding the origin of the produced geofluid.

Adding pH calculation to the media model would permit prediction of precipitation and corrosion, being a key issue in geothermal plant operation.

Coupling of a brine circuit model including heat exchanger, injection pump and injection well with existing models of reservoir (Wong et al., 2013) and power plant is planned. By replacing the usually constant boundary conditions by variables exchanged between the sub-models, their interaction can be studied in order to predict the life cycle behaviour (Blöcher, 2010).

Acknowledgements

This work was funded by the Federal Ministry of Education and Research of Germany (GeoEn II, Entwicklungsforschung im Bereich der Lagerstättenerkundung, der Bohr-, Reservoir- und Monitoring-Technologien, der Prozessmodellierung, der Material-und Korrosionsforschung und des Aufbaus

geothermischer Anlagen, Grant 03G0767A) and the Federal Ministry for the Environment, Nature Conservation and Nuclear Safety (Qualification of geothermal technology - integration of subsurface and surface systems, Grant 0325217). Special thanks go to Dr.-Ing. Thomas Reinsch and Matthis Thorade for productive discussions and corrections.

References

Ahmad, S. (1970) 'Axial Distribution of Bulk Temperature and Void Fraction in a Heated Channel With Inlet Subcooling', *Journal of Heat Transfer*, vol. 92, no. 4, p. 595, doi: 10.1115/1.3449729 .

Blöcher, G. (2010) 'Conceptual Model for Coupling Geothermal Power Plants with Deep Reservoirs', World Geothermal Congress, Bali, Indonesia 2010.

Blöcher, G., Moeck, I., Milsch, H. and Zimmermann, G. (2008) 'Modelling of pore pressure response due to hydraulic stimulation treatments at the geothermal research doublet EGRSK3/90 and GTGRSK4/05 in summer 2007', 33rd Workshop on Geothermal Reservoir Engineering, Stanford, USA.

Casas, W., Prölß, K. and Schmitz, G. (2005) 'Modeling of Desiccant Assisted Air Conditioning Systems', 4th International Modelica Conference, Hamburg University of Technology, 487-496.

Çengel, Y. (2002) *Heat Transfer: A Practical Approach*, Mcgraw-Hill.

Dassault Systèmes AB (2013) *DYMOLA*, [Online], http://www.3ds.com/products/catia/portfolio/dymola.

Driesner, T. (2007) 'The system H_2O–NaCl. Part II: Correlations for molar volume, enthalpy, and isobaric heat capacity from 0 to 1000 °C, 1 to 5000 bar, and 0 to 1 X_{NaCl}', vol. Acta 71, pp. 4902-4919.

Duan, Z. and Mao, S. (2006) 'A thermodynamic model for calculating methane solubility, density and gas phase composition of methane-bearing aqueous fluids from 273 to 523 K and from 1 to 2000 bar', *Geochimica et Cosmochimica Acta*, vol. 70, no. 13, pp. 3369-3386, doi: 10.1016/j.gca.2006.03.018 .

Duan, Z., Sun, R., Zhu, C. and Chou, I. (2006) 'An improved model for the calculation of CO2 solubility in aqueous solutions containing Na^+, K^+, Ca^{2+}, Mg^{2+}, Cl^-, and SO_4^{2-}, *Marine Chemistry*, vol. 98, no. 2-4, pp. 131-139, doi: 10.1016/j.marchem.2005.09.001 .

Dubbel (2001) *Dubbel - Taschenbuch für den Maschinenbau (20., Neubearb. U. Erw. Aufl.)*, Springer.

Elmqvist, H., Tummescheit, H. and Otter, M. (2003) 'Object-Oriented Modeling of Thermo-Fluid Systems', 3rd International Modelica Conference, Linköpings Universitet, Linköping, Sweden, pp. 269-286.

Feldbusch, E., Regenspurg, S., Banks, J., Milsch, H. and Saadat, A. (2013) 'Alteration of fluid properties during the initial operation of a geothermal plant - results from in-situ measurements in Gross Schoenebeck' (Submitted), *Environmental Earth Sciences*, SI:Geoenergy, doi 10.1007/s12665-013-2409-9 .

Francke, H. and Thorade, M. (2010) 'Density and viscosity of brine: An overview from a process engineers perspective', *Chemie der Erde – Geochemistry,* vol. 70, pp. 23-32.

Frick, S., Regenspurg, S., Kranz, S., Milsch, H., Saadat, A., Francke, H., Brandt, W. and Huenges, E. (2011) 'Geochemical and Process Engineering Challenges for Geothermal Power Generation', *Chemie Ingenieur Technik*, vol. 83, no. 12, pp. 2093-2104, doi: 10.1002/cite.201100131 .

Friedel, L. (1978) 'Druckabfall bei der Strömung von Gas/Dampf-Flüssigkeits-Gemischen in Rohren', *Chemie Ingenieur Technik*, vol. 50, no. 3, pp. 167-180, doi: 10.1002/cite.330500304 .

Gnielinski, V. (1995) 'Ein neues Berechnungsverfahren für die Wärmeübertragung im Übergangsbereich zwischen laminarer und turbulenter Rohrströmung', *Forschung im Ingenieurwesen*, vol. 61, no. 9, pp. 240-248, doi: 10.1007/BF02607964 .

Guðmundsdóttir H, Jonsson M, Palsson H (2012) Coupling wellbore simulator with reservoir simulator. In: Proceedings of 37th workshop on geothermal reservoir engineering, Stanford, California.

Haider, M. (1937) 'The Productivity Index', *Transactions of the AIME*, vol. 123, no. 1, pp. 112-119, http://www.onepetro.org/mslib/servlet/onepetropreview?id=API-36-181 .

Hasan, A. and Kabir, C. (2010) 'Modeling two-phase fluid and heat flows in geothermal wells', *Journal of Petroleum Science and Engineering*, vol. 71, no. 1-2, pp. 77-86, doi: 10.1016/j.petrol.2010.01.008 .

Henninges, J., Brandt, W., Erbas, K., Moeck, I., Saadat, A., Reinsch, T. and Zimmermann, G. (2012) 'Downhole monitoring during hydraulic experiments at the in-situ geothermal lab Gross Schönebeck', Proceedings 37th Workshop on Geothermal Reservoir Engineering, Stanford, USA, 51-56.

Huenges, E., Zimmermann, G., Reinicke, A., Blöcher, G., Holl, H., Legarth, B., Saadat, A., Möck, I., Winter, H., Brandt, W., Köhler, S., Spalek, A., Poser, M., Schrötter, J. and Becker, R. (2006) 'Technologieentwicklung im In-Situ-Geothermielabor Groß Schönebeck', in *Zweijahresbericht 2004/2005 GFZ Potsdam*, Potsdam, http://edoc.gfz-potsdam.de/gfz/8953.

Kraume, M. (2003) *Transportvorgänge in der Verfahrenstechnik: Grundlagen und apparative Umsetzungen (VDI-Buch / Chemische Technik / Verfahrenstechnik) (German Edition)*, Springer.

Laliberté, M. (2007) 'Model for Calculating the Viscosity of Aqueous Solutions', *J. Chem. Eng. Data*, vol. 52, no. 2, pp. 321-335, doi: 10.1021/je0604075.

Laliberté, M. and Cooper, E. (2004) 'Model for Calculating the Density of Aqueous Electrolyte Solutions', *J. Chem. Eng. Data*, vol. 49, no. 5, pp. 1141-1151, doi: 10.1021/je0498659 .

Livescu, S., Durlofsky, L., Aziz, K. and Ginestra, J. (2010) 'A fully-coupled thermal multiphase wellbore flow model for use in reservoir simulation', *Journal of Petroleum Science and Engineering*, vol. 71, no. 3-4, pp. 138-146, doi: 10.1016/j.petrol.2009.11.022 .

Mao, S. and Duan, Z. (2006) 'A thermodynamic model for calculating nitrogen solubility, gas phase composition and density of the N2–H2O–NaCl system', *Fluid Phase Equilibria*, vol. 248, no. 2, pp. 103-114, doi: 10.1016/j.fluid.2006.07.020 .

Mao, S. and Duan, Z. (2008) 'The P,V,T,x properties of binary aqueous chloride solutions up to T=573 K and 100 MPa', *The Journal of Chemical Thermodynamics*, vol. 40, no. 7, pp. 1046-1063, doi: 10.1016/j.jct.2008.03.005 .

Mao, S. and Duan, Z. (2009) 'The Viscosity of Aqueous Alkali-Chloride Solutions up to 623 K, 1,000 bar, and High Ionic Strength', *International Journal of Thermophysics*, vol. 30, no. 5, pp. 1510-1523, doi: 10.1007/s10765-009-0646-7.

Millero, F. (2009) 'Thermodynamic and Kinetic Properties of Natural Brines (Vol. 15, No. 1-2)', Aquatic Geochemistry, vol. 15, no. 1-2, pp. 7-41, doi: 10.1007/s10498-008-9053-0 .

Nelson, E. (1986) 'Improved cement slurry designed for thermal EOR wells', *Oil and Gas Journal*, no. 84, pp. 39-44.

Norden, B., Förster, A. and Balling, N. (2008) 'Heat flow and lithospheric thermal regime in the Northeast German Basin', *Tectonophysics*, vol. 460, no. 1-4, pp. 215-229, doi: 10.1016/j.tecto.2008.08.022 .

Norden, B., Förster, A., Behrends, K., Krause, K., Stecken, L. and Meyer, R. (2012) 'Geological 3-D model of the larger Altensalzwedel area, Germany, for temperature prognosis and reservoir simulation', *Environmental Earth Sciences*, vol. 67, no. 2, pp. 511-526, doi: 10.1007/s12665-012-1709-9 .

Ollinger, D., Baujard, C., Kohl, T. and Moeck, I. (2010) 'Distribution of thermal conductivities in the Groß Schönebeck (Germany) test site based on 3D inversion of deep borehole data', *Geothermics*, vol. 39, no. 1, pp. 46-58, doi: 10.1016/j.geothermics.2009.11.004 .

Pierrot, D. and Millero, F. (2000) 'The Apparent Molal Volume and Compressibility of Seawater Fit to the Pitzer Equations', Journal of Solution Chemistry, vol. 29, no. 8, pp. 719-742, doi: 10.1023/A:1005164911283 .

Pourafshary, P., Varavei, A., Sepehrnoori, K. and Podio, A. (2009) 'A compositional wellbore/reservoir simulator to model multiphase flow and temperature distribution', *Journal of Petroleum Science and Engineering (Vol. 69, No. 1-2)*, doi: 10.1016/j.petrol.2009.02.012.

Quong, R., Owen, L., Locke, F., Otto, Netherton, R. and Lorensen, L. (1980) 'Methane extraction from geopressured-geothermal brine at wellhead conditions', *Geothermal Resources Council Annual Meeting*, Salt Lake City.

Ramey (1962) 'Wellbore Heat Transmission', *Journal of Petroleum Technology*, vol. 14, no. 4, doi: 10.2118/96-PA .

Regenspurg, S., Wiersberg, T., Brandt, W., Huenges, E., Saadat, A., Schmidt, K. and Zimmermann, G. (2010) 'Geochemical properties of saline geothermal fluids from the in-situ geothermal laboratory Groß Schönebeck (Germany)', *Chemie der Erde - Geochemistry*, vol. 70, no. Supplement 3, pp. 3-12, doi: 10.1016/j.chemer.2010.05.002.

Reinsch, T., Henninges, J. and Aásmundsson, R. (2013) 'Thermal and chemical degradation of optical fibers (Accepted)', *Environmental Earth Sciences*, SI:Geoenergy, doi 10.1007/s12665-013-2248-8.

Sanahuja, A. and Gómez-Estévez, J. (1986) 'Determination of the enthalpies of solution at infinite dilution of KCl and NaCl in water at 303.15, 308.15, and 313.15 K', *The Journal of Chemical Thermodynamics*, vol. 18, no. 7, pp. 623-628, doi: 10.1016/0021-9614(86)90063-7 .

Scheffer, Schachtschabel, Blume, H.-P., Brümmer, G., Schwertmann, U., Horn, R., Kögel-Knabner, I., Stahr, K. and Wilke (2009) *Lehrbuch der Bodenkunde (Sav Geowissenschaften) (German Edition)*, Spektrum Akademischer Verlag.

Schön, J. (2004) *Physical Properties of Rocks, Volume 8: Fundamentals and Principles of Petrophysics (Handbook of Petroleum Exploration and Production)*, Pergamon.

Silvester, L. and Pitzer, K. (1977) 'Thermodynamics of electrolytes. 8. High-temperature properties, including enthalpy and heat capacity, with application to sodium chloride', *J. Phys. Chem.*, vol. 81, no. 19, pp. 1822-1828, doi: 10.1021/j100534a007 .

Sinke, G., Mossner, E. and Curnutt, J. (1985) 'Enthalpies of solution and solubilities of calcium chloride and its lower hydrates', *The Journal of Chemical Thermodynamics*, vol. 17, no. 9, pp. 893-899, doi: 10.1016/0021-9614(85)90083-7 .

Smith, J., Ness, H.V. and Abbott, M. (2001) *Introduction to Chemical Engineering Thermodynamics (The Mcgraw-Hill Chemical Engineering Series)*, McGraw-Hill.

Somerton, W. (1992) *Thermal Properties and Temperature-Related Behavior of Rock/Fluid Systems*, Elsevier Science, Amsterdam.

Spitzer, J., Singh, P., McCurdy, K. and Hepler, L. (1978) 'Apparent molar heat capacities and volumes of aqueous electrolytes: $CaCl_2$, $Cd(NO_3)_2$, $CoCl_2$, $Cu(ClO_4)_2$, $Mg(ClO_4)_2$, and $NiCl_2$', *Journal of Solution Chemistry*, vol. 7, no. 2, pp. 81-86, doi: 10.1007/BF00648751 .

Wagner W., Cooper J., Dittmann A., Kijima J., Kretzschmar H., Kruse A., Mareš R., Oguchi K., Sato H., Stöcker I., Šifner O., Takaishi Y., Tanishita I., Trübenbach J. and Willkommen Th (2000) 'The IAPWS Industrial Formulation 1997 for the Thermodynamic Properties of Water and Steam', *Journal of Engineering for Gas Turbines and Power*, vol. 122, no. 1, pp. 150-184, doi: 10.1115/1.483186 .

White, D., Doberstein, A., Gates, J., Tillett, D. and Wood, R. (1987) 'Heat capacity of aqueous $CaCl_2$ from 306 to 603 K at 17.5 MPa', *The Journal of Chemical Thermodynamics*, vol. 19, no. 3, pp. 251-259, doi: 10.1016/0021-9614(87)90132-7 .

White, D., Ryan, M., Armstrong, M.C., Gates, J. and Wood, R. (1987) 'Heat capacities of aqueous KCl from 325 to 600 K at 17.9 MPa', *The Journal of Chemical Thermodynamics*, vol. 19, no. 10, pp. 1023-1030, doi: 10.1016/0021-9614(87)90012-7 .

Wiersberg, T., Seibt, A. and Zimmer, M. (2004) 'Gas-geochemische Untersuchungen an Formationsfluiden des Rotliegend der Bohrung Groß Schönebeck 3/90', in Huenges, E. and Wolfgramm, M. (ed.) *Scientific Technical Report STR04/03*, Potsdam, Germany, doi: 10.2312/GFZ.b103-04036.

Wiese, B., Nimtz, M., Klatt, M. and Kühn, M. (2010) 'Sensitivities of injection rates for single well CO2 injection into saline aquifers', *Chemie der Erde - Geochemistry*, vol. 70, pp. 165-172, doi: 10.1016/j.chemer.2010.05.009 .

Willhite, P. (1967) 'Over-all Heat Transfer Coefficients in Steam And Hot Water Injection Wells', *Journal of Petroleum Technology*, vol. 19, no. 5 pp. 607–615, doi: 10.2118/1449-PA .

Wong, L., Watanabe, N., Cacace, M., Blöcher, G., Kastner, O. and Zimmermann, G. (2013) 'Sensitivity Analysis of Permeability and Apertures of Natural Internal Fault Zones on Fluid Flow and Heat Transfer in a Deep Geothermal Reservoir (Submitted)', *Environmental Earth Sciences*, SI:Geoenergy.

Yusufova, V., Pepinov, R., Nikolaev, V. and Guseinov, G. (1975) 'Thermal conductivity of aqueous solutions of NaCl', *Journal of Engineering Physics and Thermophysics*, vol. 29, no. 4, pp. 1225-1229, doi: 10.1007/BF00867119 .

Zhang, H.-L., Chen, G.-H. and Han, S.-J. (1997) 'Viscosity and Density of H2O + NaCl + CaCl2 and H2O + KCl + CaCl2 at 298.15 K', *J. Chem. Eng. Data*, vol. 42, no. 3, pp. 526-530, doi: 10.1021/je9602733.